ACS APPLIED MATERIALS & INTERFACES
www.acsami.org
Research Article

Self-Aligned Assembly of a Poly(2-vinylpyridine)-*b*-Polystyrene-*b*-Poly(2-vinylpyridine) Triblock Copolymer on Graphene Nanoribbons

Jing Zhou, Vikram Thapar, Yu Chen, Bi-Xian Wu, Gordon S. W. Craig, Paul F. Nealey, Su-Mi Hur,* Tzu-Hsuan Chang,* and Shisheng Xiong*

Cite This: *ACS Appl. Mater. Interfaces* 2021, 13, 41190–41199
Read Online

ACCESS | Metrics & More | Article Recommendations | Supporting Information

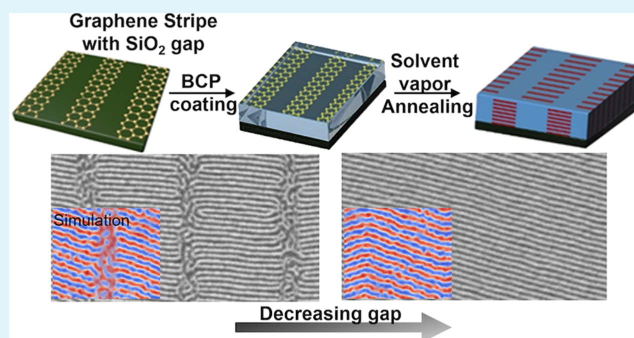

ABSTRACT: Directed self-assembly (DSA) of block copolymers is one of the most promising patterning techniques for patterning sub-10 nm features. However, at such small feature sizes, it is becoming increasingly difficult to fabricate the guiding pattern for the DSA process, and it is necessary to explore alternative guiding methods for DSA to achieve long-range ordered alignment. Here, we report the self-aligned assembly of a triblock copolymer, poly(2-vinylpyridine)-*b*-polystyrene-*b*-poly(2-vinylpyridine) (P2VP-*b*-PS-*b*-P2VP) on neutral graphene nanoribbons with the gap consisting of a P2VP-preferential silicon oxide (SiO_2) substrate via solvent vapor annealing. The assembled P2VP-b-PS-b-P2VP demonstrated long-range, one-dimensional alignment on the graphene substrate in a direction perpendicular to the boundary of the graphene and substrate with a half-pitch size of 8 nm, which greatly alleviates the lithography resolution required for traditional chemoepitaxy DSA. A wide processing window is demonstrated with the gap between graphene stripes varying from 10 to 100 nm, overcoming the restriction on widths of guiding patterns to have commensurate domain spacing. When the gap was reduced to 10 nm, P2VP-*b*-PS-*b*-P2VP formed a straight-line pattern on both the graphene and the substrate. Monte Carlo simulations showed that the self-aligned assembly of the triblock copolymer on the graphene nanoribbons is guided at the boundary of parallel and perpendicular lamellae on graphene and SiO_2, respectively. Simulations also indicate that the swelling of a system allows for rapid rearrangement of chains and quickly anneal any misaligned grains and defects. The effect of the interaction strength between SiO_2 and P2VP on the self-assembly is systematically investigated in simulations.

KEYWORDS: *graphene, triblock copolymer, solvent vapor annealing, one-dimensional assembly*

1. INTRODUCTION

Directed self-assembly (DSA) of block copolymers (BCPs) is one of the leading alternative lithography techniques, with vast potential applications in the semiconductor industry.[1−3] It features low-cost, high-resolution patterning and has versatile access to a wide range of pitch sizes. Recently, DSA has been implemented in the fabrication of ultra-high-density bit-patterned media and fin field-effect transistors (FinFETs).[4−7] It has also been employed to fabricate next-generation nonvolatile memory.[8−10] In the DSA process, BCPs undergo microphase separation and their domains can self-assemble and register to a prepatterned substrate surface to form the desired nanostructures. The common ways to guide the self-assembly of BCPs include chemoepitaxy and graphoepitaxy.[11−14] In chemoepitaxy, the alignment of the BCP domains is directed by an array of narrow guiding stripes that are separated by regions of an energetically nonpreferential surface.[15,16] Usually, these narrow guiding stripes are energetically preferential to one block in the BCP and have an optimized width that corresponds to 0.5× or 1.5× the pitch of the BCP domains, L_0. A sparse array of chemically functionalized topographic columns is used to control BCP self-assembly to form complex patterns.[17] Graphoepitaxy uses nanostructures, which are created either by etching into the underlying substrate or depositing structures on the substrate, to guide the alignment of the BCP domains within those structures.[18,19] The success of graphoepitaxy depends on the precise control of the BCP film thickness and edge roughness of the guiding nanostructures.[20] The critical dimension of the guiding pattern has to correspond to $(n - 1/2)\ L_0$. The period of the guiding structures, L_S, is an integer multiple of L_0, $L_S = DL_0$, where D is

Received: May 14, 2021
Accepted: August 4, 2021
Published: August 17, 2021

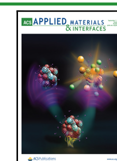

Downloaded via 73.44.161.178 on October 7, 2024 at 16:37:08 (UTC).
See https://pubs.acs.org/sharingguidelines for options on how to legitimately share published articles.

© 2021 The Authors. Published by American Chemical Society

the density multiplication factor. The development of a high-resolution DSA technique relies on continuously decreasing L_0. As a result, it is more challenging to fabricate progressively smaller guiding structures with both chemoepitaxy and graphoepitaxy.[21] More design details, including the surface topology of the created pattern,[22] interdigitation of polymer chains with grafted brush layer,[23] and the edge roughness of the guiding structures, will severely affect the perfection of BCP alignment. Therefore, it is necessary to develop alternative guiding structures for the self-assembly process that are more effective in directing the alignment of BCP domains and are easier to fabricate.

One promising method is to use two-dimensional materials, such as graphene, to replace the polymer brush that is used to make the guiding pattern. Graphene is atomically thin with a very smooth edge. The graphene surface can be chemically modified to have wetting properties similar to those of polymer brushes.[24,25] Chang et al. reported using graphene stripes as a chemical guide pattern with germanium as a neutral substrate to direct the self-assembly of polystyrene-*block*-poly(methyl methacrylate) (PS-*b*-PMMA) with D = 10.[26] The self-assembled lamellae were aligned in a direction parallel to the stripe/substrate boundary. In comparison to the chemoepitaxy using a polymer brush, their work showed faster assembly kinetics and had broader processing windows. However, the width of guiding stripes was still required to be in the vicinity of either $0.5L_0$ or $1.5L_0$. Eliminating the demand of stringent pattern size requirements, Shin et al. proposed an alternative method where the self-assembled lamellae are aligned perpendicular to the stripe/substrate boundary.[27] In their work, stripes of polymer brushes were energetically neutral to both blocks in the BCP, and these neutral stripes were then deposited on a preferential substrate. The neutral/preferential surface combination leads to the self-alignment of PS-*b*-PMMA on neutral stripes. The neutral stripe had a width of 200 nm, which was several times larger than L_0 of PS-*b*-PMMA (36 nm). This neutral/preferential interface modulation phenomenon provides an alternative solution to realize BCP alignment and greatly alleviates the requirement of making a high-resolution guide pattern for the conventional DSA process.[28]

Here, we propose using graphene nanoribbons as the neutral stripes with the gap among them consisting of the P2VP-preferential silicon oxide (SiO_2) substrate to realize one-dimensional self-aligned assembly of the triblock copolymer poly(2-vinylpyridine)-*block*-polystyrene-*block*-poly(2-vinylpyridine) (P2VP-*b*-PS-*b*-P2VP). The P2VP-*b*-PS-*b*-P2VP used in our experiment has a pitch size of 16 nm. The created graphene stripes have a width on the scale of a few hundred nanometers. We explore different processing conditions and their effects on the final morphologies of assembled P2VP-*b*-PS-*b*-P2VP. Monte Carlo (MC) simulations are used to explain the mechanism of the self-aligned assembly of the P2VP-*b*-PS-*b*-P2VP on the graphene−substrate pattern.

2. METHODS

2.1. Materials. PMMA electron beam lithography resists were purchased from Microchem. $FeCl_3$, acetone, isopropyl alcohol (IPA), methyl isobutyl ketone (MIBK), trimethylaluminum (TMA, 96%), toluene, and PMMA were purchased from Sigma-Aldrich and used as received. Styrene, 2-vinylpyridene monomer, and a random copolymer of styrene and 2-vinylpyridine (PS-*r*-P2VP, M_n = 30 kg/mol) were purchased from Polymer Source and used as received. Cross-linkable PS, with glycidyl methacrylate (GMA) as a cross-linking agent, was provided by AZ Electronic Materials. P2VP-*b*-PS-*b*-P2VP triblock copolymers (8k-17k-8k, L_0 = 16 nm) were synthesized via living anionic polymerization using a bifunctional initiator with the sequential addition of styrene followed by 2-vinylpyridine.

2.2. Preparation of the Graphene Chemical Pattern on the SiO_2/Si Substrate. A monolayer of graphene was deposited on a Cu foil using a customized chemical vapor deposition (CVD) tool. The graphene synthesis process is similar to that previously reported.[26] A piece of Cu foil was annealed at 1200 °C with 4 sccm of H_2 gas at 40 mTorr for 10 min, followed by 50 sccm of CF_4 gas at 40 mTorr for 30 min. To transfer the as-grown graphene monolayer, a thin layer of PMMA was spin-coated on the deposited graphene. After dissolving the Cu foil in an $FeCl_3$ solution (0.05 M), the obtained graphene/PMMA thin film was transferred to a SiO_2/Si substrate. The PMMA layer was completely removed through a rinsing process (acetone, isopropyl alcohol, and deionized water). Before patterning the graphene, the sample was annealed at 300 °C for 2 h at $\sim 10^{-6}$ mTorr. This temperature heating process was repeated until all of the organic residues in graphene were completely removed by thermal decomposition. Electron beam lithography was used to produce a chemical pattern on the graphene. A 95 nm-thick film of photoresist (PMMA 950 A2) was spin-coated onto the graphene at 4000 rpm and baked at 180 °C for 3 min. The photoresist was patterned with a scanning electron microscope (SEM, LEO-1, aperture 10 μm, 20 keV) and developed for 30 s in MIBK/IPA and rinsed for another 30 s in IPA. The pattern on the exposed photoresist was then transferred to the underlying graphene with an oxygen plasma etch in a reactive ion etching (RIE) tool (Unaxis 790 Series) at 50 W and 10 sccm O_2 for 3 s. The residue of photoresist was stripped with chlorobenzene. Finally, the graphene chemical pattern was thermally annealed at 350 °C for 2 h under vacuum to complete the preparation. The thickness of the graphene chemical pattern was measured with an atomic force microscope (AFM, Veeco MultiMode SPM). The obtained graphene pattern was imaged with an SEM (Zeiss SUPRA 60).

2.3. Solvent Vapor Annealing of P2VP-*b*-PS-*b*-P2VP on the Graphene Chemical Pattern. P2VP-*b*-PS-*b*-P2VP (1 wt % in toluene) was spin-coated on the patterned graphene stripes. The thickness of the P2VP-*b*-PS-*b*-P2VP thin film ($\sim 1L_0$) was measured by both ellipsometry and AFM. The solvent annealing process was carried out in a customized chamber using acetone as the annealing solvent, and nitrogen was used as the carrier and diluting gas.[29] Mass flow controllers (5−500 sccm) were applied to accurately control the amount of acetone vapor in the chamber. Reflectometry (Filmetrics 60) was used to monitor the P2VP-*b*-PS-*b*-P2VP film thickness in situ during the solvent annealing process. After solvent annealing, the acetone vapor was vented by purging with nitrogen continuously for 5 min.

2.4. Pattern Transfer to the Underlying Silicon Substrate. Sequential infiltration synthesis (SIS) was used to form AlO_x in the P2VP domains of self-assembled P2VP-*b*-PS-*b*-P2VP.[30−32] The SIS process was performed with an atomic layer deposition (ALD) tool (Fiji F200, Cambridge Nanotech/Ultratech). Self-assembled P2VP-*b*-PS-*b*-P2VP samples were placed in the ALD chamber, which was purged with Ar at a flow rate of 20 sccm for 5 min to reduce its impurities and moisture content. Two precursors, trimethylaluminum (TMA) and H_2O were introduced into the ALD chamber through different valves at room temperature in an alternate mode at 90 °C. During the deposition, the reaction between TMA and H_2O occurred preferentially in the P2VP domain. After each TMA/H_2O deposition cycle, a purge-and-wait step (5 min) was applied to allow the complete reaction of two precursors inside the P2VP domains, while removing the byproducts. In our case, we completed the SIS process with three cycles of TMA/H_2O deposition. After SIS, the P2VP-*b*-PS-*b*-P2VP template was removed by O_2 RIE for 300 s. The remaining AlO_x patterns, which replicated the P2VP microdomains, were used as a hard mask for pattern transfer into the Si substrates. The Si substrate was etched by RIE with CF_4/CHF_3 gas, and the residual AlO_x was dissolved in a NaOH bath at room temperature.

2.5. Monte Carlo Simulations. The model used in this work relies on a particle-based representation of copolymer molecules, which has been described extensively in the literature[33−35] and

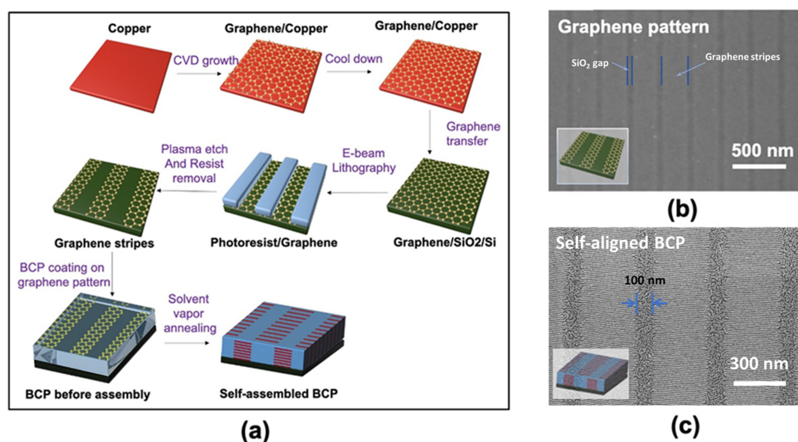

Figure 1. Process flow of self-assembly of a block copolymer (BCP) on graphene chemical patterns on a Si/SiO_2 substrate. (a) Schematic of the generation of the graphene-based chemical pattern and subsequent self-assembly of the triblock copolymer on graphene chemical patterns. (b) SEM image of patterned graphene stripes, with the accompanying schematic in the lower-left corner. (c) SEM image of a self-aligned BCP on graphene stripes, whose width is 300 nm and the gap between two graphene stripes is 100 nm. The schematic in the lower-left corner shows the orientation of the domains relative to the graphene nanoribbons and the exposed substrate.

validated with available experimental data for copolymer thin films.[36−43] Here, we only mention the model's main characteristics that are used to simulate our system of interest. All n A-*b*-B-*b*-A block copolymer chains in our system are in a constant volume and constant temperature environment and discretized into N beads. The bonded interactions are derived from harmonic springs attached between adjacent beads in a given chain. The total harmonic potential H_b at a given temperature T for the above system is defined as

$$H_b = \frac{3k_bT}{2}\frac{N-1}{\mathrm{Re}^2}\sum_{k=1}^{n}\sum_{i=1}^{N-1} b_k^2(i) \tag{1}$$

where $\mathbf{b}_k(i)$ is a vector connecting ith and $(i+1)$th bead in chain k, R_e is the mean-squared end-to-end distance for an isolated non-interacting chain, and k_b is the Boltzmann constant. The nonbonded interactions, H_{nb}, modeled in this work are expressed as a functional of local densities, $\phi_A(\mathbf{r})$ and $\phi_B(\mathbf{r})$. These densities, as discussed later, are estimated from bead positions. The nonbonded interactions are given by

$$\frac{H_{nb}[\phi_A, \phi_B]}{k_BT} = \sqrt{\bar{N}}\int_V \frac{\mathrm{d}r}{R_e^3}\left[\chi N\phi_A\phi_B + \frac{\kappa N}{2}(1-\phi_A-\phi_B)^2\right] \tag{2}$$

where the first term represents the incompatibility between A and B beads and is proportional to the segregation strength, χN, which is the product of the Flory−Huggins interaction parameter, χ, and the number of segments in the polymer chain, N. The second term, which is derived from the Helfand quadratic approximation, restricts the fluctuations of local densities away from the average value and is proportional to product κN, where κ is the incompressibility parameter. The term $\sqrt{\bar{N}}$ is an interdigitation parameter that provides an estimate of the number of chains with which a given chain interacts.

To calculate H_{nb}, the local densities must be inferred from the beads' positions. A commonly used "particle-to-mesh" (PM) technique is applied, where we split the simulation box into M number of cubic grid cells and estimate the densities of species in these grids. The grid discretization length is defined as ΔL. The implementation details are discussed by Detcheverry et al.[43] The local density for the grid cell p, $\phi_\alpha(p)$ ($\alpha \in$ {A,B}), is defined as

$$\phi_\alpha(p) = \frac{R_e^3}{\Delta L^3 N\sqrt{\bar{N}}}\sum_{i=1}^{nN}\delta(\mathbf{r}_i - \mathbf{r}(p))\delta_{\alpha t(i)} \tag{3}$$

where the above summation runs over all beads, and $t(i)$ denotes the species of bead, i. The delta function here represents that each bead is assigned to its nearest grid cell and contributes to $\phi_\alpha(p)$.

In the experimental study, the substrate and stripe regions at the bottom are also interacting with beads. To include these interactions in a model, the following potential is added to the model:[44]

$$H_s = \frac{\lambda}{d_s/\mathrm{Re}}\sum_i \exp\left[-\frac{z_i^2}{2d_s^2}\right] \tag{4}$$

where z_i is the vertical distance of ith bead from the bottom. The potential decays over a short distance $d_s = 0.15R_e$ and the strength of the interaction between the bottom surface and the BCP is characterized by the product λN, where λ represents the interfacial energy between the surface and a segment of the polymer. In this work, both the A and B blocks of the BCP can interact with both the substrate gap (SiO_2/Si) and the stripe (graphene) region, resulting in four potential strengths of interaction denoted by $\lambda_{\text{A-stripe}}N$, $\lambda_{\text{B-stripe}}N$, $\lambda_{\text{A-substrate}}N$, and $\lambda_{\text{B-substrate}}N$. Their values are adjusted such that the substrate is preferential to A and the stripe is nonpreferential to B. The values used for $\lambda_{\text{A-stripe}}N$, $\lambda_{\text{B-stripe}}N$, $\lambda_{\text{A-substrate}}N$, and $\lambda_{\text{B-substrate}}N$ are 0, 0, −0.65, and 0, respectively.

Having defined our model, we perform MC simulations with an NVT ensemble. In this simulation technique, a move is proposed where a randomly selected bead or a collection of beads are displaced from their original positions. The difference between the energy of the new configuration and the original configuration is estimated, which then determines the probability of accepting the move. The acceptance probability is determined by the Metropolis criterion, which is given by min $[1, \exp(-\Delta E/k_BT)]$. In this work, two types of moves are used, single-bead displacement and chain reptation. In a bead displacement move, we randomly select a bead and propose a move in all three directions by random amounts in the range of $[-\mathrm{d}q, \mathrm{d}q]$. The value $\mathrm{d}q$ is set as $0.8b$, where b is the mean square bond length of an ideal chain. In a reptation move, we randomly select a chain and propose a move in which m randomly chosen beads are selected from either end of the chain and then reattached to the opposite end of the chain ($m \leq 5$). In this work, an MC cycle consists of $nN + 2n$ MC moves, where on average nN bead displacement moves and $2n$ reptation moves are performed.

The values of κN, χN, $\sqrt{\bar{N}}$, and ΔL are set to 50, 35, and $0.16R_e$, respectively. To capture the screening of polymer−polymer interactions by solvents in our implicit solvent model, a lower $\sqrt{\bar{N}}$ value is used for a low swelling ratio (L-SWR) system than for a high swelling ratio (H-SWR) system. Specifically, the $\sqrt{\bar{N}}$ values used for

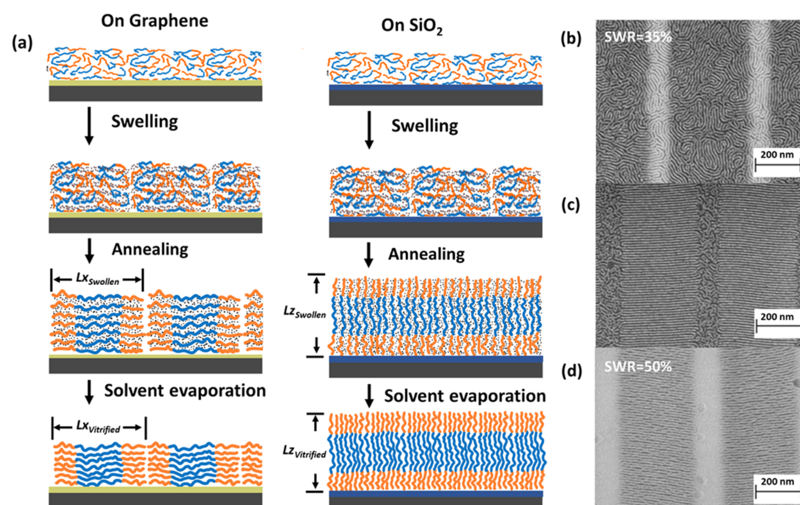

Figure 2. (a) Schematic of solvent vapor annealing (SVA) on a graphene stripe and SiO_2 gap. SVA of P2VP-*b*-PS-*b*-P2VP (8k-17k-8k) with different swelling ratios of (b) 35%, (c) 45%, and (d) 50% in an acetone atmosphere. The SEM images are taken after the SIS process.

H-SWR and L-SWR are 120 and 60, respectively. The simulation box sizes in the x and y directions are chosen to be $14L_0$ and $10L_0$, respectively, where L_0 is equated to $1.25R_e$. The values of the simulation box in the z-direction for the H-SWR and L-SWR systems are selected to be $1.5R_e$ and $1.3R_e$, respectively.

3. RESULTS AND DISCUSSION

A schematic illustration of the process for generating the graphene nanoribbons on a substrate and then using them for DSA of the BCP is presented in Figure 1a. Graphene was grown with CVD on a copper film and then transferred to a silicon oxide wafer. E-beam lithography was used to pattern the graphene film into lines, as shown in the SEM image in Figure 1b. The BCP was spin-coated onto the patterned wafer and, subsequently, solvent annealed in acetone to drive the self-assembly of the BCP on the graphene nanoribbons. Above the nanoribbons, the BCP self-assembled with the lamellae oriented perpendicular to the substrate, and the lamellae ran orthogonal to the direction of the nanoribbons, as shown in the SEM image in Figure 1c. In contrast to the lamellae above the graphene, the lamellae above the exposed substrate portion of the chemical pattern self-assembled in a disordered pattern.

It is of great importance to explore the effects of process parameters, such as solvent vapor annealing (SVA) conditions and the geometry of the graphene pattern, on the self-assembly of P2VP-*b*-PS-*b*-P2VP on the graphene guide pattern. We first explored the influence of SVA conditions on the final pattern of P2VP-*b*-PS-*b*-P2VP on the graphene guide pattern. In this experiment, the patterned graphene stripes have a width of 300 nm and the gap between the two graphene stripes is 100 nm. The SVA process is schematically depicted in Figure 2a. Briefly, during the SVA process, the absorption of annealing solvent in P2VP-*b*-PS-*b*-P2VP swells the polymer and effectively lowers its glass transition temperature (T_g) by weakening the polymer−polymer interactions, which greatly increase the polymer chain mobility and therefore accelerates the self-assembly of P2VP-*b*-PS-*b*-P2VP.[45] In this experiment, acetone vapor was used as the annealing agent for P2VP-*b*-PS-*b*-P2VP, and the amount of acetone vapor in the annealing chamber was controlled by adjusting the flow rates of diluting gas (N_2) and carrier gas (N_2). The swelling ratio (SWR) of P2VP-*b*-PS-*b*-P2VP was obtained by measuring the changes of P2VP-*b*-PS-*b*-P2VP film thickness during SVA (SWR = $(t_{SWOLLEN} - t_{AS\text{-}CAST})/t_{AS\text{-}CAST}$) and was proportional to the amount of acetone vapor in the chamber. The self-assembly results of P2VP-*b*-PS-*b*-P2VP at different SWRs are demonstrated in Figure 2b−d. It was found that at a low acetone flow rate (SWR = 35%) on both a neutral graphene stripe and a P2VP-selective SiO_2 substrate, P2VP-*b*-PS-*b*-P2VP self-assembled into a perpendicular lamellar fingerprint structure, which was the same as self-assembly of P2VP-*b*-PS-*b*-P2VP on an unpatterned graphene substrate (Figure S1, Supporting Information). However, when SWR was increased to 45%, P2VP-*b*-PS-*b*-P2VP achieved ordered, one-dimensional self-alignment on the graphene stripes, whereas perforated lamellar-like structures were observed on the SiO_2 substrate. As seen in Figure 2c, the observed one-dimensional alignment is long-ranged and is at a direction perpendicular to the graphene/SiO_2 boundary. As explained later in detail through simulations, such direction of alignment is guided by Scherk surfaces, which is the morphology obtained by combining two planes that are perpendicular to each other.[27] In this work, Scherk surfaces formed at the interfaces of the parallelly aligned lamellae on the SiO_2 and the perpendicularly aligned lamellae on the graphene. The increase in the mobility of chains due to the swelling helped in the rapid rearrangement of chains along the Scherk surface-guided direction of alignment, resulting in the long-range ordering over the large graphene stripe widths. One-dimensional alignment of P2VP-*b*-PS-*b*-P2VP on graphene stripes could also be obtained at higher SWR (SWR = 50%), but defects, such as bridging, appeared at a higher acetone flow rate. The vapor pressure of the solvent controls the thickness of the swollen film and thus the relative concentrations of the polymer and solvent in the film. The rate of the ordered phase growth is the product of two terms, a polymer relaxation rate and a thermodynamic driving force. A higher concentration of solvent results in faster chain dynamics but also lowers the driving force for the growth of a particular ordered state. Therefore, at the same annealing temperature and time, there are more defects at SWR = 50% than at 45%. Therefore, it is important to control the amount of acetone vapor in P2VP-*b*-PS-*b*-P2VP to obtain a defect-free, one-dimensional, self-aligned nanopattern. Based on our experiment, the SWR should be controlled to ∼45% to realize defect-

https://doi.org/10.1021/acsami.1c08940
ACS Appl. Mater. Interfaces 2021, 13, 41190−41199

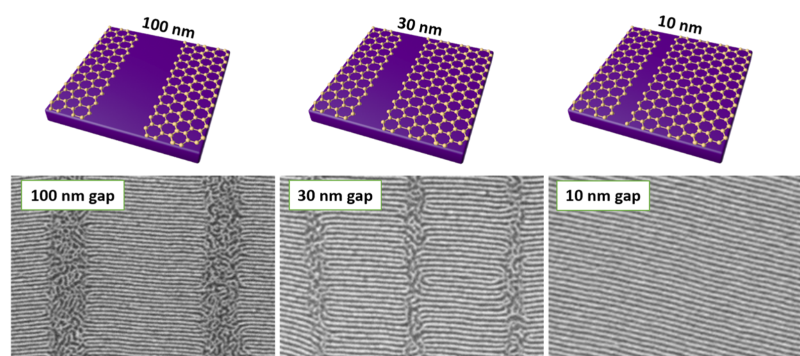

Figure 3. Solvent vapor annealing of P2VP-*b*-PS-*b*-P2VP (8k-17k-8k) on graphene stripes with different gap widths, indicated by the labels on the top row and shown in the corresponding schematics. The SEM images in the bottom row were taken after the SIS process.

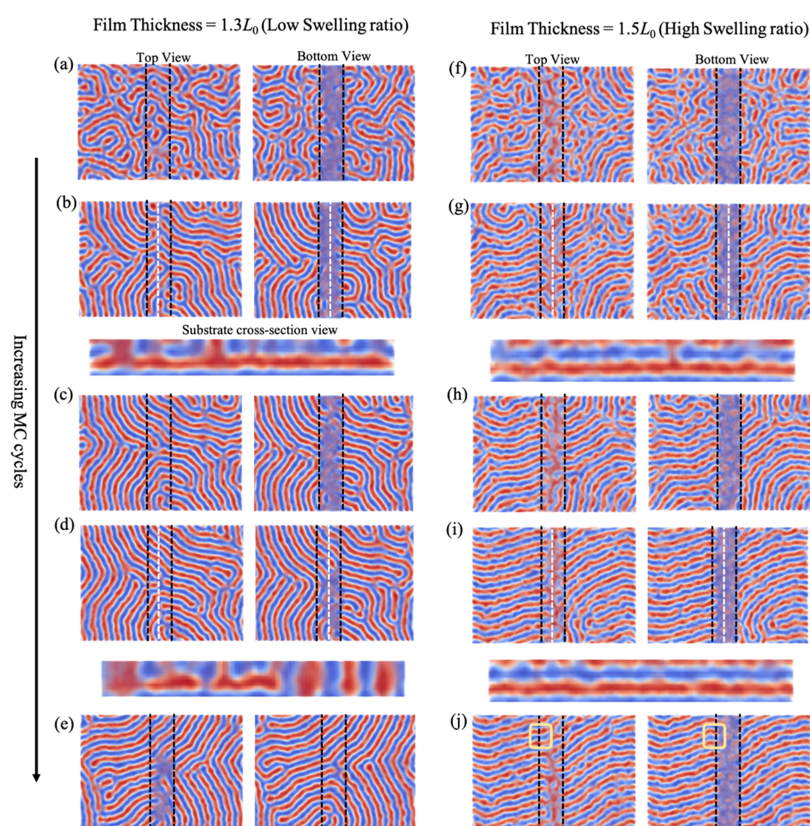

Figure 4. Subfigures (a)−(e) and (f)−(j) show the obtained BCP morphologies on a stripe/substrate template with the substrate placed at a template center in our MC simulations for L-SWR (film thickness = 1.3L_0) and H-SWR (film thickness = 1.5L_0) systems, respectively, as they approach equilibrium. The subfigures (a)−(e) are morphologies obtained at 10^4, 4 × 10^4, 9 × 10^4, 1.75 × 10^5, and 3.95 ×10^5 MC cycles, respectively, whereas the subfigures (f)−(j) are morphologies obtained at 10^4, 2.5 × 10^4, 4 × 10^4, 4.15 × 10^5, and 5.8 × 10^5 MC cycles, respectively. For each subfigure, the top and bottom views of each morphology are shown. For subfigures (b), (d), (g), and (i), cross-section views along the dotted white line (middle of the substrate region) are also shown labeled as substrate cross-section view in subfigure (b). The dotted black lines in the top and bottom views represent the left and right locations of the substrate region. A-rich and B-rich domains are represented by red and blue colors, respectively. The yellow boxes in the top and bottom views in subfigure (j) are drawn to depict the location of boundary edges of Scherk surfaces. For both systems, the width of the substrate region, i.e., the gap between the stripes, is 2L_0.

free, one-dimensional self-alignment of P2VP-*b*-PS-*b*-P2VP on graphene stripes.

After the optimization of the annealing conditions, we further explored the impact of the graphene guide pattern on the self-assembly of P2VP-*b*-PS-*b*-P2VP. Three sets of graphene guide patterns with the same stripe width (300 nm) but with different gap widths (100, 30, and 10 nm) were prepared. After spin-coating the P2VP-*b*-PS-*b*-P2VP films, these samples were annealed in acetone at the optimized SWR (45%). The annealed samples were characterized by SEM after the SIS process, as shown in Figure 3. The micronscale SEM images are also provided in Figure S2 of the Supporting Information. It was observed that when the gap width was 100 or 30 nm, P2VP-*b*-PS-*b*-P2VP could self-assemble into one-dimensional, self-aligned lamellar patterns on the graphene stripes with a perforated lamellar-like structure on the SiO_2 substrate. Interestingly, when the gap was reduced to 10 nm, P2VP-*b*-PS-*b*-P2VP formed a straight-line pattern on both the

https://doi.org/10.1021/acsami.1c08940
ACS Appl. Mater. Interfaces 2021, 13, 41190−41199

substrate and stripe. At a gap of 10 nm, the width of the exposed SiO_2 area was comparable to half the pitch size of the block copolymer, and thus the entire surface corresponded to the P2VP-preferential SiO_2 substrate inserted between the neutral graphene surface stripes. Such bottom surfaces with regularly placed neutral and $\sim 0.5L_0$ preferential regions are similar to guiding substrates used in conventional chemo-epitaxy DSA processes. However, as shown in Figure 3, self-assembled P2VP-*b*-PS-*b*-P2VP lamellae in this study are not aligned parallel to the neutral/preferential surface boundary as in the case of chemoepitaxy; they tend to align in a direction perpendicular to the boundary similar to the results obtained for larger gaps. This observation is further discussed later with the help of simulations.

To study the mechanism of the self-assembly of the triblock copolymers on the graphene patterns with different gap widths, we applied a theoretically informed coarse-grained (TICG) implicit solvent model[46,47] in combination with MC simulations. TICG is a particle-based model in which each chain is represented by a number N of coarse-grained beads. The model was used to understand the self-assembly of a generic A-*b*-B-*b*-A BCP (where A and B are different blocks) on a generic stripe/substrate system placed at the bottom surface (for details, see the Methods section). The simulated stripe, substrate, A, and B corresponded to graphene, the SiO_2 substrate, P2VP, and PS, respectively, in the experiments. As mentioned in the Methods section, the relevant interactions described in our model were (i) the bonded interactions of polymer chains adapting a Gaussian random-walk configuration of coarse-grained polymer beads, (ii) interactions due to incompatibility between unlike beads, (iii) an energy penalty due to the deviation of local bead densities away from the average value, and (iv) the interactions between stripe/substrate and beads. These interactions were parameterized by the model parameters, $\sqrt{\bar{N}}$, χN, κN, and λN. The interaction strengths of the stripe and substrate surfaces with each polymer block were adjusted to reproduce the experimental preferentiality of the SiO_2 substrate to P2VP and the neutrality of the graphene stripe toward both PS and P2VP blocks. Annealing of a disordered A-*b*-B-*b*-A film coated onto a stripe/substrate template with the substrate placed at a template center was simulated by performing a combination of single-bead displacements and reptation moves. Further model and MC simulation details, including relevant equations to describe all interactions and values of model parameters, are provided in the Methods section.

Figure 4 shows the self-assembled morphologies after solvent annealing of a P2VP-*b*-PS-*b*-P2VP film with an initial thickness of L_0 at different swelling ratios. The addition of solvent swells the P2VP-*b*-PS-*b*-P2VP thin film, thereby screening out the interactions among polymers. The weakening of the polymer−polymer interactions lowers its glass transition temperature and increases chain mobility. The increase in SWR not only increases the screening effect of polymer−polymer interactions but also increases the overall film thickness. To mimic these experimental conditions, we conducted simulations for two different systems: a system with $1.3L_0$ swollen film thickness of a lower swelling ratio (L-SWR) and a system with $1.5L_0$ film thickness of a high swelling ratio (H-SWR), representing the low (35%) and high (45%) SWR experimental conditions, respectively. The weakening of interactions among polymer chains upon swelling is reflected by setting a smaller interdigitation number $\sqrt{\bar{N}}$ for the H-SWR system compared to the L-SWR system in our implicit solvent model while keeping the other model parameters fixed (the values of model parameters are given in the Methods section). Smaller $\sqrt{\bar{N}}$ values imply that a given polymer bead interacts with fewer neighboring beads, which effectively captures the screening of interactions by the solvent. The width of the substrate region, i.e., the gap between the stripes, is set to $2L_0$. The dotted black lines drawn in Figure 4 represent the left and right boundaries of the substrate region. Figure 4a−e and Figure 4f−j show the L-SWR and H-SWR systems, respectively, after different numbers of iterations of our MC simulations as they approach equilibrium. For each figure, top and bottom views of each morphology are shown. Cross-section views along the dotted white line (middle of the substrate region) are shown in Figure 4b,d,g,i. A-rich and B-rich regions are represented by red and blue colors, respectively. In both systems, randomly placed beads with fixed bond lengths are used as an initial configuration.

In the L-SWR simulation, at the early iterations shown in Figure 4a,b, the A block wets the A-selective bottom substrate and surface-parallel lamellae are formed. The cross-section view in Figure 4b shows alternating A and B domains across the film thickness, whereas the randomly oriented surface-perpendicular lamellae are observed on the neutral stripe. However, during the equilibration process of the L-SWR system, the initially formed parallel lamellae on the substrate are unstable due to chain stretching/compression required for stabilizing the parallel lamellae at an incommensurate film thickness of $1.3L_0$. Thus, the parallel lamellae strive to reshape into perpendicular lamellae, as shown in the top and bottom views in Figure 4c,d. Also, as clearly depicted in the cross-section view of Figure 4d, perpendicularly aligned grains are developed, including the area near the substrate. Also, the weakened segregation strength caused by the solvent screening effect and the enhanced chain mobility in the swollen state enables the polymer chains to rearrange from parallel lamellae into perpendicular lamellae over a small number of MC iterations. Therefore, as shown in Figure 4e, a fingerprint-like structure is observed from the top; the observed result matches with the experimental result for low swelling ratios of 35% (Figure 2a).

Similar to the L-SWR system, the H-SWR system forms parallel and perpendicular morphologies on the substrate and stripe regions, respectively, at the early stage of the simulations, as observed in Figure 4f,g. The alternating A and B domains in the cross-section view along the middle of the substrate are shown in Figure 4g. In the H-SWR system, parallel lamellae on the substrate region are stable because of the commensurate film thickness of $1.5L_0$. As discussed in Shin et al., the most stable morphology at the interface connecting the parallel and perpendicular lamellae is referred to as a Scherk surface morphology.[27] The Scherk surfaces lower the interfacial energy penalty of the system and can act as a guiding template to uniformly align the perpendicular lamellae on the neutral stripe region in the direction orthogonal to the stripe/substrate boundaries. Randomly oriented perpendicular lamellae with multiple grains can be clearly observed from Figure 4f−h. Also, misaligned grains are quickly annealed during our simulation (see Figure 4h,j) because the H-SWR system allows for the rapid rearrangement of polymer chains in pursuit of a uniformly aligned structure on the stripe region. During the

https://doi.org/10.1021/acsami.1c08940
ACS Appl. Mater. Interfaces 2021, 13, 41190−41199

course of the MC simulations, fluctuations are observed at the edge locations of the perpendicular lamellae (*i.e.*, the location of the boundary edges of the Scherk surfaces). Two such edges are highlighted in the yellow box in the top and bottom views of Figure 4j. While the nonselective top surface allows such edges to penetrate in the substrate region (inside the black dashed lines) due to the thermodynamic driving force toward uniformly aligned perpendicular lamellae, the chemical contrasts at the substrate pin down the edges' position near the bottom at the boundary of the stripe and the substrate, limiting the extent of penetrations and preventing the formation of perpendicular lamellae over the whole domain. Instead, perforated lamellar-like structures are observed, similar to what was seen in the experiments. It is also notable that there exist fluctuations in the orientation of the perpendicularly aligned structure on the stripe region.

The tilted orientation in simulations, as depicted in Figure 4j, is partially due to the limited number of cycles performed to equilibrate the system. Figure S3a,b of the Supporting Information shows that on increasing the number of cycles, defects get further annihilated and lamellae are oriented further in a direction orthogonal to the stripe/substrate boundary.

Another reason for tilting is the lack of registration of A/B domains at Scherk surfaces. The lamellae ends are pinned along the stripe/substrate interfaces through Scherk surfaces. When the vertical positions of pinning locations of a left interface are not in coordination with a right interface, it could result in slight tilting of aligned lamellae. For comparison, the cropped SEM image highlighting the interface of a couple of aligned lamellae with dotted black lines is shown in Figure S3c. Finding a method to provide registration of the domain and controlling the slight tilting is our planned future work.

Similar to the experiments, the effect of the gap between the stripes is investigated via simulations of varying widths of the substrate region in the center of our simulation box. Figure 5a shows the top views of the equilibrated morphology for three different widths. In all cases, Scherk surfaces uniformly align

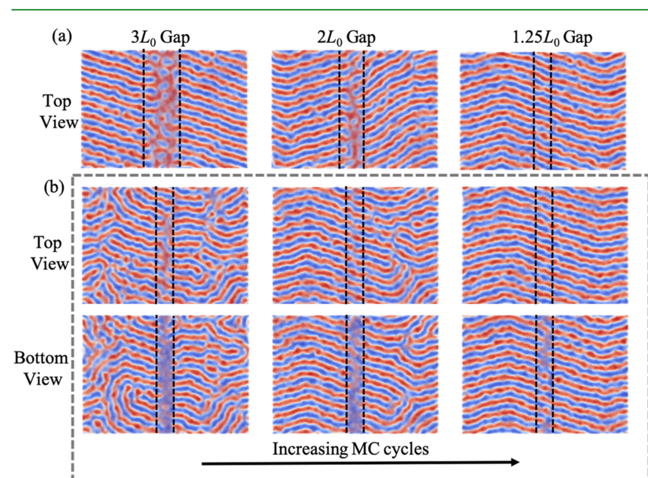

Figure 5. (a) Top views of the equilibrated morphologies for three different substrate widths (i.e., gap between stripes): 3, 2, and $1.25L_0$. (b) In the gray dotted box, the BCP morphology changes during the equilibration of the $1.25L_0$ system. From left to right, the shown morphologies are obtained at 2.5×10^4, 9×10^4, and 1.585×10^6 MC cycles. Both top and bottom views of each morphology are shown. The A-rich and B-rich domains are represented by red and blue colors, respectively.

the perpendicular domains on the stripe region. Notably, because these Scherk surfaces occur at the interface between the perpendicular and parallel domains regardless of the gap size, they should be effective in aligning the domains even for significantly larger gap sizes. When the width of the substrate gap is large ($3L_0$), parallel lamellae on the substrate region are favorable and perforated AB domains on the substrate region are observed from the top, which is similar to the experimental observations. In contrast, when the width of the substrate gap is small ($1.25L_0$), as viewed from the top, uniformly aligned lamellae are observed across the top surface, as is observed experimentally (the rightmost figure in Figure 3). The orientation of the lamellae is orthogonal to the stripe/substrate boundary, unlike the normal chemoepitaxy DSA, in which the stripe guides the orientation of the ordered phase. Bezik et al.[47] recently reported that the free energy difference between the orthogonal and parallel alignment of the lamellae is small in comparison to the large energy barriers separating the two states. Thus, once the orthogonally aligned lamellae are kinetically trapped, they can be long-lasting within a reasonable process time. To further understand the formation of the surface-perpendicular lamellae that are aligned orthogonally to the stripe/substrate boundaries, morphologies at different stages of MC simulations during the equilibration are shown in Figure 5b. The leftmost part of Figure 5b shows the early stage when Scherk surfaces are formed by reorienting perpendicular lamellae that were initially randomly oriented. Shown in the middle and right top view of Figure 5b, surface-perpendicular grains at the left and right boundaries of the substrate/stripe become aligned along the same direction and are connected, thereby decreasing the AB interfacial area. Concomitant with the fluctuations in the boundary edge locations of the Scherk surfaces, the uniform one-directionally aligned assembly obtained at the top then endeavors to propagate throughout the film (see bottom views of middle and right subfigures in Figure 5b).

We further investigate the effect of the surface interaction strength on the assembly by conducting simulations for different $\lambda_{\text{A-substrate}}N$. Figure S4 shows the obtained morphologies for both L-SWR and H-SWR conditions from the system of $2L_0$ gap and $\lambda_{\text{A-substrate}}N$ values of −0.1, −0.4, −0.7, and −1.0. The values of −0.1 and −0.4 are not strong enough to stabilize the parallel lamellae on the substrate region at the early stage of structure evolution and result in fingerprint perpendicular lamellae over both neutral and weakly selective domains, as shown in the top and bottom views of morphologies (Figure S4a,b,e,f). At a moderate $\lambda_{\text{A-substrate}}N$ value of −0.7, the obtained results are similar to Figure 4 of $\lambda_{\text{A-substrate}}N$ = 0.65. On further increasing $\lambda_{\text{A-substrate}}N$ to −1.0, for the L-SWR system, perpendicular lamellae are viewed from the top (Figure S4d) on the substrate region, but they do not strive to be throughout the film as the B block prefers to be fully wetted by the substrate because of strong attraction among them. Therefore, parallelly aligned lamellae are observed on the substrate region when viewed from the bottom. In the case of the H-SWR system, the strongly preferential substrate shows a similar result as that of the moderately preferential substrate with aligned lamellae directed by Scherk surfaces. However, for smaller gaps of $1.25L_0$, the strongly preferential substrate ($\lambda_{\text{A-substrate}}N$ = −1.0) does not result in the experimentally observed perpendicular assembly throughout the film on both stripe and substrate regions (see Figure S5). Instead, identical to the systems on the graphene

https://doi.org/10.1021/acsami.1c08940
ACS Appl. Mater. Interfaces 2021, 13, 41190−41199

with wider gaps, perforated lamellae are observed on the substrate gap.

4. CONCLUSIONS

In this work, we used the bottom surface of graphene stripes with the gap among them consisting of P2VP-preferential silicon oxide (SiO_2) substrate to direct the self-assembly of a P2VP-*b*-PS-*b*-P2VP. The P2VP-*b*-PS-*b*-P2VP successfully formed sub-10 nm one-dimensional lamellar nanostructures on the graphene stripes with a SVA process. We also explored the influence of various solvent annealing conditions and the geometry of the graphene guide pattern on the final morphology of assembled P2VP-*b*-PS-*b*-P2VP and obtained the optimized processing window to obtain a defect-free pattern. MC simulations were performed to understand the mechanism of automatic, one-dimensional self-alignment of the triblock copolymer on the graphene stripes. Simulations show that the Scherk surfaces formed at the boundary of parallel and perpendicular lamellae on graphene and SiO_2, respectively, act as a guiding template to uniformly align the perpendicular lamellae on the neutral stripe region in the direction orthogonal to the stripe/substrate boundaries. Simulations also indicate that when swelling ratios correspond to commensurate film thickness, the swelling of a system allows for rapid rearrangement of chains and quickly anneal any misaligned grains and defects.

Our work using two-dimensional materials for the Scherk surface-induced assembly has been shown as a viable solution for a sub-10 nm DSA process in this work. Guiding the assembly using Scherk surfaces has been explored previously. However, the aligned assembly reported in earlier works is only on the neutral stripe while the gap region has the parallel assembly. In this work, with a reduced gap size, we have achieved a well-aligned lamella over a large area both on the stripe and substrate. In conventional chemoepitaxy, which allows large area aligned pattern formation, the critical dimension of the guiding pattern features has to correspond to $(n - 1/2)L_0$. Therefore, it is difficult to fabricate such features, if we want to achieve BCP assemblies with sub-10 nm domains via chemoepitaxy. Moreover, at sub-10 nm scales, line-edge and surface roughness of the guiding features can become significant compared to L_0, disrupting BCP registration. Our approach removes this stringent requirement on the size of guiding features and does not require that L_S of the guide pattern is commensurate to L_0 of the BCP. Graphene is robust to a broad range of manufacturing conditions with strong thermal and mechanical properties. The use of a smooth, flat, and rigid surface of graphene as a patterning material provides perfect 2D chemical contrast on the bottom and enables a long-ranged straight-line pattern over a large area with a half-pitch size of 8 nm. We believe that our method demonstrates a facile solution to pattern sub-10 nm features that should work with a broad variety of BCPs and therefore has the potential to broaden the scope of use of BCPs in electronic device manufacturing.

■ ASSOCIATED CONTENT

Supporting Information

The Supporting Information is available free of charge at https://pubs.acs.org/doi/10.1021/acsami.1c08940.

SEM image of self-aligned BCP P2VP-*b*-PS-*b*-P2VP on unpatterned graphene stripes; micronscale SEM images of solvent vapor annealing of P2VP-*b*-PS-*b*-P2VP on graphene stripes with different gap widths; top views of the obtained BCP morphologies on a stripe/substrate template with the substrate placed at a template center in MC simulations for the H-SWR system with $2L_0$ gap; the obtained BCP morphologies on a stripe/substrate template with the substrate placed at a template center in our MC simulations for L-SWR and H-SWR systems, respectively, for different $\lambda_{\text{A-substrate}}N$ values (PDF)

■ AUTHOR INFORMATION

Corresponding Authors

Su-Mi Hur − *School of Polymer Science and Engineering, Chonnam National University, Gwangju 61186, Korea*; orcid.org/0000-0002-6101-3142; Email: shur@chonnam.ac.kr

Tzu-Hsuan Chang − *Graduate Institute of Electronics Engineering, National Taiwan University, Taipei 106, Taiwan*; Email: tchang9@ntu.edu.tw

Shisheng Xiong − *School of Information Science and Technology, Fudan University, Shanghai 200433, China*; Email: sxiong@fudan.edu.cn

Authors

Jing Zhou − *School of Information Science and Technology, Fudan University, Shanghai 200433, China*

Vikram Thapar − *School of Polymer Science and Engineering, Chonnam National University, Gwangju 61186, Korea*; orcid.org/0000-0002-5415-3737

Yu Chen − *School of Information Science and Technology, Fudan University, Shanghai 200433, China*

Bi-Xian Wu − *Graduate Institute of Electronics Engineering, National Taiwan University, Taipei 106, Taiwan*

Gordon S. W. Craig − *Pritzker School of Molecular Engineering, University of Chicago, Chicago, Illinois 60637, United States*

Paul F. Nealey − *Pritzker School of Molecular Engineering, University of Chicago, Chicago, Illinois 60637, United States*; orcid.org/0000-0003-3889-142X

Complete contact information is available at: https://pubs.acs.org/10.1021/acsami.1c08940

Author Contributions

J.Z. and V.T. contributed equally to this work. The manuscript was written through contributions of all authors. All authors have given approval to the final version of the manuscript.

Funding

This work is financially supported by the National Natural Science Foundation of China (No. 61974030), the Shanghai Municipal Science and Technology Commission (No. 18500745900). V.T. and S.-M.H. acknowledge funding support by the National Research Foundation of Korea (NRF) grant funded by the Korean government (MSIT) (2018R1A5A 1025224 and 2018H1D3A1A01036430). The work at National Taiwan University (NTU) has been supported by the Ministry of Science and Technology (109-2222-E-002-002-MY3) and the Ministry of Education through the Higher Education Sprout Projects (NTU core consortium: 109L891606).

Notes

The authors declare no competing financial interest.

REFERENCES

(1) Stoykovich, M. P.; Kang, H.; Daoulas, K.Ch.; Liu, G.; Liu, C.-C.; de Pablo, J. J.; Müller, M.; Nealey, P. F. Directed Self-Assembly of Block Copolymers for Nanolithography: Fabrication of Isolated Features and Essential Integrated Circuit Geometries. *ACS Nano* **2007**, *1*, 168−175.

(2) Bates, C. M.; Maher, M. J.; Janes, D. W.; Ellison, C. J.; Willson, C. G. Block copolymer lithography. *Macromolecules* **2014**, *47*, 2−12.

(3) Jeong, S.-J.; Xia, G.; Kim, B. H.; Shin, D. O.; Kwon, S.-H.; Kang, S.-W.; Kim, S. O. Universal Block Copolymer Lithography for Metals, Semiconductors, Ceramics, and Polymers. *Adv. Mater.* **2008**, *20*, 1898−1904.

(4) Xiong, S.; Chapuis, Y.-A.; Wan, L.; Gao, H.; Li, X.; Ruiz, R.; Nealey, P. F. Directed self-assembly of high-chi block copolymer for nano fabrication of bit patterned media via solvent annealing. *Nanotechnology* **2016**, *27*, No. 415601.

(5) Liu, C.-C.; Franke, E.; Mignot, Y.; Xie, R.; Yeung, C. W.; Zhang, J.; Chi, C.; Zhang, C.; Farrell, R.; Lai, K.; Tsai, H.; Felix, N.; Corliss, D. Directed self-assembly of block copolymers for 7 nanometre FinFET technology and beyond. *Nat Electron* **2018**, *1*, 562−569.

(6) Hellwig, O.; Bosworth, J. K.; Dobisz, E.; Kercher, D.; Hauet, T.; Zeltzer, G.; Risner-Jamtgaard, J. D.; Yaney, D.; Ruiz, R. Bit patterned media based on block copolymer directed assembly with narrow magnetic switching field distribution. *Appl. Phys. Lett.* **2010**, *96*, No. 052511.

(7) Park, S.; Lee, D. H.; Xu, J.; Kim, B.; Hong, S. W.; Jeong, U.; Xu, T.; Russell, T. P. Macroscopic 10-Terabit-per-Square-Inch Arrays from Block Copolymers with Lateral Order. *Science* **2009**, *323*, 1030−1033.

(8) Park, W. I.; You, B. K.; Mun, B. H.; Seo, H. K.; Lee, J. Y.; Hosaka, S.; Yin, Y.; Ross, C. A.; Lee, K. J.; Jung, Y. S. Self-Assembled Incorporation of Modulated Block Copolymer Nanostructures in Phase-Change Memory for Switching Power Reduction. *ACS Nano* **2013**, *7*, 2651−2658.

(9) You, B. K.; Park, W. I.; Kim, J. M.; Park, K.; Seo, H. K.; Lee, J. Y.; Jung, Y. S.; Lee, K. J. Reliable Control of Filament Formation in Resistive Memories by Self-Assembled Nanoinsulators Derived from a Block Copolymer. *ACS Nano* **2014**, *8*, 9492−9502.

(10) Frascaroli, J.; Brivio, S.; Lupi, F. F.; Seguini, G.; Boarino, L.; Perego, M.; Spiga, S. Resistive Switching in High-Density Nanodevices Fabricated by Block Copolymer Self-Assembly. *ACS Nano* **2015**, *9*, 2518−2529.

(11) Kim, S. O.; Solak, H. H.; Stoykovich, M. P.; Ferrier, N. J.; de Pablo, J. J.; Nealey, P. F. Epitaxial self-assembly of block copolymers on lithographically defined nanopatterned substrates. *Nature* **2003**, *424*, 411−414.

(12) Segalman, R. A.; Yokoyama, H.; Kramer, E. J. Graphoepitaxy of Spherical Domain Block Copolymer Films. *Adv. Mater.* **2001**, *13*, 1152−1155.

(13) Ryu, D. Y.; Shin, K.; Drockenmuller, E.; Hawker, C. J.; Russell, T. P. A. Generalized Approach to the Modification of Solid Surfaces. *Science* **2005**, *308*, 236−239.

(14) Bita, I.; Yang, J. K. W.; Jung, Y. S.; Ross, C. A.; Thomas, E. L.; Berggren, K. K. Graphoepitaxy of self-assembled block copolymers on two-dimensional periodic patterned templates. *Science* **2008**, *321*, 939−943.

(15) Chan, B. T.; Tahara, S.; Parnell, D.; Rincon Delgadillo, P. A.; Gronheid, R.; Marneffe, J.-F. de.; Xu, K.; Nishimura, E.; Boullart, W. 28nm pitch of line/space pattern transfer into silicon substrates with chemo-epitaxy Directed Self-Assembly (DSA) process flow. *Microelectron. Eng.* **2014**, *123*, 180−186.

(16) Segal-Peretz, T.; Ren, J.; Xiong, S.; Khaira, G.; Bowen, A.; Ocola, L. E.; Divan, R.; Doxastakis, M.; Ferrier, N. J.; Pablo, J.; de Nealey, P. F. Quantitative Three-Dimensional Characterization of Block Copolymer Directed Self-Assembly on Combined Chemical and Topographical Prepatterned Templates. *ACS Nano* **2017**, *11*, 1307−1319.

(17) Chang, J.-B.; Choi, H. K.; Hannon, A. F.; Alexander-Katz, A.; Ross, C. A.; Berggren, K. K. Design rules for self-assembled block copolymer patterns using tiled templates. *Nat. Commun.* **2014**, *5*, No. 3305.

(18) Tang, Q.; Ma, Y. High density multiplication of graphoepitaxy directed block copolymer assembly on two-dimensional lattice template. *Soft Matter* **2010**, *6*, 4460−4465.

(19) Jeong, S.-J.; Kim, J. E.; Moon, H.-S.; Kim, B. H.; Kim, S. M.; Kim, J. B.; Kim, S. O. Soft Graphoepitaxy of Block Copolymer Assembly with Disposable Photoresist Confinement. *Nano Lett.* **2009**, *9*, 2300−2305.

(20) Barros, P. P.; Gharbi, A.; Fouquet, A.; Bos, S.; Hazart, J.; Delachat, F.; Chevalier, X.; Cayrefourcq, I.; Pain, L.; Tiron, R. Balancing Block Copolymer Thickness over Template Density in Graphoepitaxy Approach. *Macromol. Mater. Eng.* **2017**, *302*, No. 1700285.

(21) Liu, C.-C.; Han, E.; Onses, M. S.; Thode, C. J.; Gopalan, S.; Ji, P.; Nealey, P. F. Fabrication of Lithographically Defined Chemically Patterned Polymer Brushes and Mats. *Macromolecules* **2011**, *44*, 1876−1885.

(22) Selkirk, A.; Prochukhan, N.; Lundy, R.; Cummins, C.; Gatensby, R.; Kilbride, R.; Parnell, A.; Vasquez, J. B.; Morris, M.; Mokarian-Tabari, P. Optimization and Control of Large Block Copolymer Self-Assembly via Precision Solvent Vapor Annealing. *Macromolecules* **2021**, *54*, 1203−1215.

(23) Gu, X.; Gunke, I.; Hexemer, A.; Gu, W.; Russell, T. P. An In Situ Grazing Incidence X-Ray Scattering Study of Block Copolymer Thin Films During Solvent Vapor Annealing. *Adv. Mater.* **2014**, *26*, 273−281.

(24) Kim, B. H.; Kim, J. Y.; Jeong, S.-J.; Hwang, J. O.; Lee, D. H.; Shin, D. O.; Choi, S.-Y.; Kim, S. O. Surface Energy Modification by Spin- Cast, Large-Area Graphene Film for Block Copolymer Lithography. *ACS Nano* **2010**, *4*, 5464−5470.

(25) Lee, C.; Wei, X.; Kysar, J. W.; Hone, J. Measurement of the Elastic Properties and Intrinsic Strength of Monolayer Graphene. *Science* **2008**, *321*, 939−943.

(26) Chang, T.-H.; Xiong, S.; Jacobberger, R. M.; Mikael, S.; Suh, H. S.; Liu, C.-C.; Geng, D.; Wang, X.; Arnold, M. S.; Ma, Z.; Nealey, P. F. Directed self-assembly of block copolymer films on atomically-thin graphene chemical patterns. *Sci. Rep.* **2016**, *6*, No. 31407.

(27) Shin, D. O.; Kim, B. H.; Kang, J.-H.; Jeong, S.-J.; Park, S. H.; Lee, Y.-H.; Kim, S. O. One-Dimensional Nanoassembly of Block Copolymers Tailored by Chemically Patterned Surfaces. *Macromolecules* **2009**, *42*, 1189−1193.

(28) Gottlieb, S.; Fernández-Regúlez, M.; Lorenzoni, M.; Evangelio, L.; Perez-Murano, F. Grain-Boundary-Induced Alignment of Block-Copolymer Thin Films. *Nanomaterials* **2020**, *10*, No. 103.

(29) Xiong, S.; Li, D.; Hur, S.-M.; Craig, G. S. W.; Arges, C. G.; Qu, X.-P.; Nealey, P. F. The Solvent Distribution Effect on the Self-Assembly of Symmetric Triblock Copolymers during Solvent Vapor Annealing. *Macromolecules* **2018**, *51*, 7145−715.

(30) Tseng, Y.-C.; Peng, Q.; Ocola, L. E.; Elam, J. W.; Darling, S. B. Enhanced Block Copolymer Lithography Using Sequential Infiltration Synthesis. *J. Phys. Chem. C* **2011**, *115*, 17725−17729.

(31) Waldman, R. Z.; Jeon, N.; Mandia, D. J.; Heinonen, O.; Darling, S. B.; Martinson, A. B. F. Sequential infiltration synthesis of electronic materials: Group 13 oxides via metal alkyl precursors. *Chem. Mater.* **2019**, *31*, 5274−5285.

(32) Lee, S.-M.; Pippel, E.; Moutanabbir, O.; Kim, J.-H.; Lee, H.-J.; Knez, M. In situ Raman spectroscopic study of Al-infiltrated spider dragline silk under tensile deformation. *ACS Appl. Mater. Interfaces* **2014**, *6*, 16827−16834.

(33) Detcheverry, F. A.; Kang, H.; Daoulas, K. C.; Müller, M.; Nealey, P. F.; de Pablo, J. J. Monte Carlo Simulations of a Coarse Grain Model for Block Copolymers and Nanocomposites. *Macromolecules* **2008**, *41*, 4989−5001.

(34) Detcheverry, F. A.; Pike, D. Q.; Nagpal, U.; Nealey, P. F.; de Pablo, J. J. Theoretically Informed Coarse Grain Simulations of Block Copolymer Melts: Method and Applications. *Soft Matter* **2009**, *5*, 4858−4865.

https://doi.org/10.1021/acsami.1c08940
ACS Appl. Mater. Interfaces 2021, 13, 41190−41199

(35) Ramírez-Hernández, A.; Detcheverry, F. A.; Peters, B. L.; Chappa, V. C.; Schweizer, K. S.; Müller, M.; de Pablo, J. J. Dynamical Simulations of Coarse Grain Polymeric Systems: Rouse and Entangled Dynamics. *Macromolecules* **2013**, *46*, 6287−6299.

(36) Detcheverry, F. A.; Pike, D. Q.; Nealey, P. F.; Müller, M.; de Pablo, J. J. Monte Carlo Simulation of Coarse Grain Polymeric Systems. *Phys. Rev. Lett.* **2009**, *102*, No. 197801.

(37) Detcheverry, F. A.; Liu, G.; Nealey, P. F.; de Pablo, J. J. Interpolation in the Directed Assembly of Block Copolymers on Nanopatterned Substrates: Simulation and Experiments. *Macromolecules* **2010**, *43*, 3446−3454.

(38) Hur, S.-M.; Thapar, V.; Ramírez-Hernández, A.; Khaira, G.; Segal-Peretz, T.; Rincon-Delgadillo, P. A.; Li, W.; Müller, M.; Nealey, P. F.; de Pablo, J. J. Molecular Pathways for Defect Annihilation in Directed Self-Assembly. *Proc. Natl. Acad. Sci. U.S.A.* **2015**, *112*, 14144−14149.

(39) Jacobberger, R. M.; Thapar, V.; Wu, G.-P.; Chang, T.-H.; Saraswat, V.; Way, A. J.; Jinkins, K. R.; Ma, Z.; Nealey, P. F.; Hur, S.-M.; Xiong, S.; Michael, S. Boundary-directed epitaxy of block copolymers. *Nat. Commun.* **2020**, *11*, No. 4151.

(40) Liu, G.; Delcambre, S. P.; Stuen, K. O.; Craig, G. S. W.; de Pablo, J. J.; Nealey, P. F.; et al. Mechanism and dynamics of block copolymer directed assembly with density multiplication on chemically patterned surfaces. *J. Vac. Sci. Technol. B* **2010**, *28*, C6B13−C6B19.

(41) Nagpal, U.; Müller, M.; Nealey, P. F.; de Pablo, J. J. Free Energy of Defects in Ordered Assemblies of Block Copolymer Domains. *ACS Macro Lett.* **2012**, *1*, 418−422.

(42) Hur, S.-M.; Thapar, V.; Ramírez-Hernandez, A.; Nealey, P. F.; de Pablo, J. J. Defect Annihilation Pathways in Directed Assembly of Lamellar Block Copolymer Thin Films. *ACS Nano* **2018**, *12*, 9974−9981.

(43) Detcheverry, F. A.; Kang, H.; Daoulas, K. C.; Müller, M.; Nealey, P. F.; de Pablo, J. J. Monte Carlo Simulations of a Coarse Grain Model for Block Copolymers and Nanocomposites. *Macromolecules* **2008**, *41*, 4989−5001.

(44) Daoulas, K. C.; Müller, M.; de Pablo, J. J.; Nealey, P. F.; Smith, G. D. Morphology of multi-component polymer systems: single chain in mean field simulation studies. *Soft Matter* **2006**, *2*, 573−583.

(45) Matsen, M. W. Architectural Effect on the Surface Tension of an ABA Triblock Copolymer Melt. *Macromolecules* **2010**, *43*, 1671−1674.

(46) Detcheverry, F. A.; Pike, D. Q.; Nagpal, U.; Nealey, P. F.; de Pablo, J. J. Theoretically Informed Coarse Grain Simulations of Block Copolymer Melts: Method and Applications. *Soft Matter* **2009**, *5*, 4858−4865.

(47) Bezik, C. T.; de Pablo, J. J. Formation, Stability, and Annihilation of the Stitched Morphology in Block Copolymer Thin Films. *Macromolecules* **2020**, *53*, 10446−10456.

https://doi.org/10.1021/acsami.1c08940
ACS Appl. Mater. Interfaces 2021, 13, 41190−41199